Measurement of magnetostatic mode excitation and relaxation in permalloy films using scanning Kerr imaging

S. Tamaru* and J. A. Bain
The Data Storage Systems Center, Carnegie Mellon University, Pittsburgh, Pennsylvania 15213, USA

R. J. M. van de Veerdonk, T. M. Crawford, M. Covington, and M. H. Kryder
Seagate Research, Pittsburgh, Pennsylvania 15222, USA

(Received 17 February 2004; revised manuscript received 12 May 2004; published 24 September 2004)

This work presents experimental results of magnetostatic mode excitation using scanning Kerr microscopy under continuous sinusoidal excitation in the microwave frequency range. This technique was applied to 100 nm thick permalloy coupons excited in two different ways. In the first experiment, the uniform (Kittel) mode was excited at frequencies in 2.24–8.00 GHz. The resonant condition was effectively described with the conventional Kittel mode equation. The LLG damping parameter α increased significantly with decreasing bias field. It was confirmed that this increase was caused by multidomain structure and ripple domains formed under weak bias fields, as suggested by other studies. In the second experiment, propagating magnetostatic mode surface waves were excited. They showed an exponential amplitude decay and a linear phase variation with distance from the drive field source, consistent with a decaying plane wave. The Damon-Eshbach (DE) model was extended to include a finite energy damping and used to analyze the results. It was found that the wave number and the decay constant were reasonably well described by the extended DE model. In contrast to the first experiment, no significant variation of α with frequency or bias field was seen in this second experiment, where spatial inhomogeneities in the magnetization are less significant.

DOI: 10.1103/PhysRevB.70.104416 PACS number(s): 75.30.Ds, 76.50.+g

I. INTRODUCTION

The interest in magnetization dynamics is currently being driven by the development of various high speed magnetic devices such as magnetic heads for hard disk drives and MRAM. These applications require very fast, often subnanosecond magnetization reversals in soft magnetic transition metals. The dynamics of a magnetic moment behaving in a coherent fashion are expressed by the Landau-Lifshitz-Gilbert (LLG) equation[1]

$$\frac{d\vec{M}}{dt} = -\gamma\vec{M}\times\vec{H} + \frac{\alpha}{M}\vec{M}\times\frac{d\vec{M}}{dt}, \tag{1}$$

where γ is the gyromagnetic constant given as $g\mu_B\mu_0/\hbar$, g is Lande g factor, μ_B is the Bohr magneton, $\hbar$ is Planck's constant divided by 2π, μ_0 is the permeability of vacuum, $\vec{M}$ is the magnetization, $\vec{H}$ is the magnetic field, and α is the phenomenological damping parameter. In this equation, the first and the second terms represent the precessional motion and the energy dissipation, respectively. It can be shown from Eq. (1) that the magnetization switching rate is greatly affected by the energy dissipation rate, represented by α. Therefore, estimation of α and understanding of underlying physics concerning the energy dissipation mechanism are crucial for the development of high speed magnetic devices.

There are a number of studies that have estimated the damping parameter in transition metal systems using various techniques. In the frequency domain, ferromagnetic resonance (FMR) has been most commonly used for determining α in the relatively high frequency region (typically above several GHz).[2–4] In the low-frequency region (below a few GHz), α has been measured by using a permeance meter.[5–7] In the time domain, α has been estimated by exciting a magnetic thin film with a step pulse or impulse field and capturing the decaying free oscillation of the magnetization with an inductive[8–11] or optical[10,12] apparatus. These measurements usually come up with a value of α for evaporated or sputtered permalloy films within the range of 0.005–0.02 depending on the measurement condition and the sample configuration.

Generally, most FMR measurements have concluded that the damping parameter α is independent of frequency over the relevant measurement range,[2] while low frequency permeance measurements have suggested that α becomes larger as the frequency is reduced, possibly due to the magnetization ripple or inhomogeneity of the local magnetization.[6,13] Inductive time domain measurements have also shown a similar behavior in the low bias field region. Additionally, these measurements showed correlation between the increase of α and the higher order magnetostatic mode excitations, suggesting that these magnetostatic modes may play an important role in the energy dissipation process.[8,10,14]

Damon and Eshbach obtained a solution for the magnetostatic mode waves propagating in a magnetic slab.[15] This DE model has been widely used as the theoretical basis in this field. Experimentally, yttrium-iron-garnet (YIG) has been most commonly used as the magnetic slab for the study of magnetic excitations since this material has a very small energy damping and therefore magnetostatic mode waves can propagate over very long distances, often millimeters. However, the DE model assumes absolutely no energy damping. Also, very few of the past experimental studies of the magnetic excitations in YIG have addressed the decay of magne-

tostatic mode waves. Hence these studies can not provide enough information about the relaxation of magnetostatic mode waves.

When excitation is accomplished with spatially uniform fields (as in conventional FMR) and the response is averaged over a relatively large area of the sample, the sensitivity for higher order modes tends to drop significantly. In this case, elucidation of the energy flow from the excitation field into various modes of magnetic excitation becomes model dependent, particularly with regard to higher order modes. Also, magnetic excitations in heavily damped systems should quickly decay as they propagate. Therefore, it is difficult to study such spatially varying magnetic excitations without spatial resolution capability. For these reasons, it is highly desirable to directly excite a mode of interest selectively with a localized field source and measure its properties in detail with spatial resolution in order to better understand the magnetic excitation and relaxation processes. This allows direct observation of dynamic behavior and reduces dependence on dynamic models. Recent work in this vein has been carried out by using propagating spin wave spectroscopy (PSWS),[16] time domain inductive measurements,[14] and time resolved (TR) scanning Kerr effect microscopy (SKEM).[17,18]

We have recently introduced a variation on TR-SKEM for performing microscopic FMR, namely spatially resolved ferromagnetic resonance (SRFMR) SKEM.[19] This technique allows one to capture both the spatial distribution of the amplitude and phase of the magnetization response with picosecond temporal resolution and optical diffraction limited spatial resolution. This capability makes this technique particularly useful for studying magnetic excitations in heavily damped systems. In this work, measurements of magnetic excitation in permalloy films were carried out by using SRFMR-SKEM in two canonical geometries, excitation of a uniform precession (Kittel) mode and plane magnetostatic mode surface waves (MSSW's) propagating in one dimension. The resonant condition and the damping behavior in the uniform excitation are analyzed by the conventional Kittel mode equation, and the modified Polder susceptibility tensor theory, respectively. The properties of the propagating MSSW's are analyzed by the Damon-Eshbach (DE) model extended to include the influence of a finite damping parameter.

II. EXPERIMENTAL

Details of the SRFMR-SKEM system have been presented elsewhere.[19] A block diagram of the measurement setup is shown in Fig. 1(a). A Ti: sapphire mode-locked laser generates an optical pulse train with a wavelength of 400 nm and a pulse width of 1.5 ps precisely synchronized to the 80 MHz reference signal. An rf synthesizer generates a sinusoidal HF signal whose phase is also precisely locked to the reference signal. It has been confirmed that the total timing jitter of this system is less than 5 ps, small enough to work up to frequencies of several GHz. The HF signal is sent to a coplanar transmission line of the integrated sample situated beneath the magnetic sample. The drive field generated by the HF signal flowing into the transmission line excites the

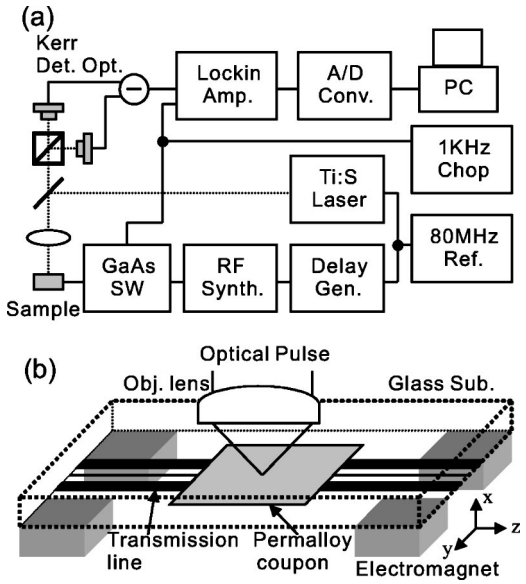

FIG. 1. Schematic diagram of the SRFMR-SKEM setup. (a) Entire system and (b) integrate sample.

magnetic sample while the optical pulses illuminate the sample stroboscopically at one phase point of the HF signal. The reflected optical pulses have a slightly rotated polarization plane proportional to the polar magnetization due to the polar Kerr effect. This Kerr rotation is detected by differential Kerr detection optics composed of a Glan laser calcite polarizer and two photodiodes. The HF signal is chopped at 1 kHz by a GaAs switch and the frequency component of this chop signal in the photoinduced current is extracted by a lock-in amplifier. Thus, this system measures the difference of the polar Kerr signal between the excited and unexcited states. By changing the relative timing between the optical pulse and the HF signal, the wave form of the magnetization response over one entire cycle of the HF signal is captured. Repeating the process at a series of points, while scanning over the sample, allows the spatial distribution of the magnetization response to be mapped.

Two integrated samples with different geometries were prepared in this work to study the magnetic excitation under different conditions. Sample 1 is a 50 μm$\times$50 μm square permalloy coupon with a coplanar transmission line having 600 μm total and 100 μm center conductor widths. Sample 2 is a 1 mm$\times$1 mm square coupon with 18 μm total and 3 μm center conductor widths. These samples are constructed by first sputter depositing a 100 nm thick permalloy layer on a glass substrate and photolithographically patterning it into the square shapes with the sizes described above. An insulation layer of 540 nm thick alumina is next deposited on the magnetic layer. On top of this structure is formed a coplanar transmission line of 750 nm thick copper having a characteristic impedance of 50 Ω and the conductor widths as specified above. The adoption of coplanar transmission line geometry allows us to fabricate a wide variety of drive field sources on one wafer only by defining the geometries on the photomask without changing the thickness of the insulation layer which would be required in the microstrip geometry. BH loop tracer measurements on the permalloy film

before patterning showed that the film has a uniaxial anisotropy H_k of about 320 A/m(4 Oe) along the transmission line direction. The saturation magnetization of the permalloy layer M_S was estimated as 7.96×10^5 A/m (B_S=1.00 T) by SQUID measurement.

This sample is mounted on an electromagnet that generates a dc bias field along the transmission line. During measurement, a bias field of 9.12×10^4 A/m (1.15 kOe) is first applied to saturate the sample, then the field is reduced to the measurement point. This consistent field application history ensures a repeatable static domain structure. A relatively low power objective lens having a numerical aperture (NA) of 0.25 was used in this study for focusing the laser pulse in order to suppress the peak power density at the center of the optical spot under the damage threshold without reducing the total optical power. Using the equation for estimating the full width at half maximum (FWHM) d of an optical spot $d=0.61\lambda/NA$, a spatial resolution of about 1.0 μm is expected in the current optical configuration, fine enough for imaging the samples with the sizes specified above. Coordinate axes used in the following discussion are defined as shown in Fig. 1(b), as is a schematic of the sample geometry. The SI unit system is followed throughout this paper.

III. RESULTS AND DISCUSSION

A. Sample 1 (uniform excitation)

The center conductor of sample 1 is twice as wide as the square size of the magnetic coupon. A calculation of the drive field profile assuming a uniform current density in the conductor estimates the maximum field variation to be less than 3%. This reasonably uniform drive field should efficiently couple to the uniform (Kittel) mode. Figure 2 shows the amplitude and phase of the magnetization response normal to the film plane at the center of the magnetic coupon excited by 7.04 GHz HF drive field as a function of bias field. One caution in the phase plot is that the system is not calibrated to give the absolute phase with respect to the drive field. Therefore the phase value may have an arbitrary offset. A large peak is seen in the amplitude plot, which is the resonant peak of the lowest order mode in this sample. Figure 3 shows the relation between the excitation frequency and the bias field at the resonant peak. The resonant condition of the uniform (Kittel) mode in a thin film under the condition of $H_B+H_k \ll M_S$ is given by[8]

$$(2\pi f_p)^2 = \gamma^2 M_S(H_B + H_k), \tag{2}$$

where f_p is the resonant frequency, H_B is the bias field, H_k is the uniaxial anisotropy field, and M_S is the saturation magnetization, respectively. Assuming that the observed peak follows the above behavior, the resonant condition was analyzed by using this equation with g and H_k as fitting parameters. The result of fitting is also shown as a solid line in Fig. 3. The agreement between the theory and the experimental data is good, yielding a g value of 2.16 and H_k of 1.24×10^3 A/m(15.6 Oe). This g value is fairly consistent with the value widely accepted by the FMR community, but somewhat lower than that obtained on almost identical

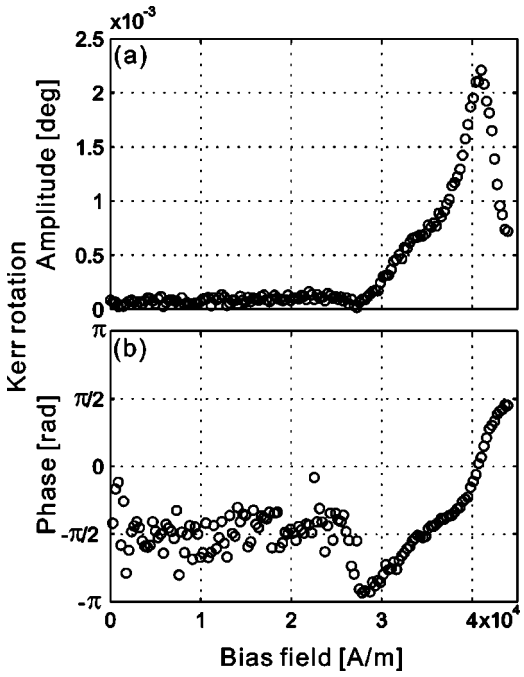

FIG. 2. Magnetization response at the center of the 50 μm $\times$50 μm square permalloy coupon (sample 1) as a function of bias field. (a) and (b) show the amplitude and phase variation, respectively. The excitation is accomplished by a 7.04 GHz uniform HF drive field.

samples using inductive technique (g=2.26).[14] We attribute this difference to errors in the bias field calibration in the SRFMR-SKEM system. The observed difference between g =2.16 and 2.26 corresponds to an calibration error of about 9%. This is probably due to some uncertainty of the sample placement in a rather localized dc bias field generated by an iron core electromagnet used in this system, while the inductive technique reported in Ref. [14] uses a Helmholtz coil to generate a very uniform bias field. However, the value of g =2.16 will be used to keep the consistency with other parameters in the following discussion.

There are couple of possible sources which may cause the difference between H_k as determined from the static measurement of 320 A/m and the above value. The first is the

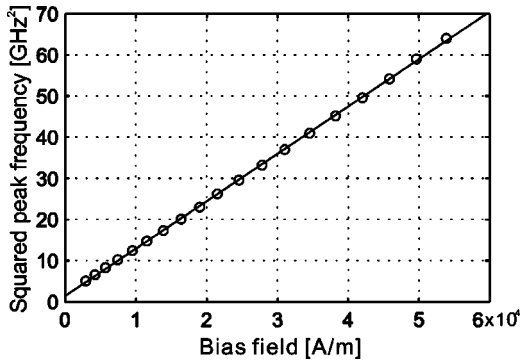

FIG. 3. Dependence of squared excitation frequency on the bias field at the resonant peak. The open circles and the solid line show the experimental results and the theoretical values calculated by Eq. (2) with g=2.16 and $H_k=1.24\times10^3$ A/m, respectively

shape induced anisotropy as a result of patterning into a square shape which has fourfold symmetry. The second is the dynamic demagnetization factor caused by a nonuniform distribution of the precession amplitude.[8,20] Actually, the value of $H_k = 1.24 \times 10^3$ A/m is in reasonable agreement with the value obtained on an identical sample by inductive technique, which can be accounted for by employing the mode quantization condition of the MSSW and an appropriate boundary condition.[11]

As can be seen in Fig. 2(b), the phase variation is well behaved and monotonic around the peak. Further analysis of the energy damping within the resonant peak is possible using this information about the phase variation of the magnetization precession. As the first step, the magnetization dynamics of the lowest resonant mode at the center of the sample are assumed to be similar to the ideal Kittel mode and therefore can be expressed by the LLG equation (1). Note that this is clearly an approximation because the magnetization in sample 1 at resonance is not precessing as a single, uniform moment, but has some spatial variation which becomes larger as the bias field decreases (as shown later). However, this approximation is supported by the fact that the resonant condition is well described by the conventional Kittel mode equation. By assuming that the exchange field is much smaller than the bias field and therefore negligible, the total magnetic field is given by

$$\vec{H} = \vec{H}_e + \vec{H}_k - N_d \vec{M}, \tag{3}$$

where $\vec{H}_e$ is the total external field and N_d is the demagnetization tensor. The field and the magnetization can be decomposed into a static part and a dynamic part. The static part of the magnetization, the external bias field and the uniaxial anisotropy field are all aligned with the z axis, and N_d can be approximated as having only one nonzero component along the x axis in the geometry of sample 1 (normal to the film). Therefore, these quantities can be expressed as

$$\vec{H}_e + \vec{H}_k = (H_B + H_k)\vec{e}_z + \vec{h}\exp(-i\omega t), \tag{4}$$

$$\vec{M} = M_S \vec{e}_z + \vec{m}\exp(-i\omega t), \tag{5}$$

$$N_{d,nn} = \begin{cases} 1 & (nn = xx) \\ 0 & (\text{others}) \end{cases}, \tag{6}$$

where $\vec{e}_z$ is the unit vector along the z axis, $\vec{m}$ and $\vec{h}$ are the amplitude vectors of the dynamic magnetization and the dynamic external field, respectively, and ω is the angular frequency of the drive field. In this measurement, it is assumed that the magnitudes of the dynamic terms $|\vec{m}|$ and $|\vec{h}|$ are much smaller than the static terms and they have only x and y components. Plugging Eqs. (3)–(6) into Eq. (1) and dropping the second order terms yields the modified Polder susceptibility tensor for thin films P':[21]

$$\vec{m} = P'\vec{h},$$

$$P' = \zeta \begin{pmatrix} \omega_0 - i\alpha\omega & -i\omega \\ i\omega & \omega_0 - i\alpha\omega + \omega_M \end{pmatrix},$$

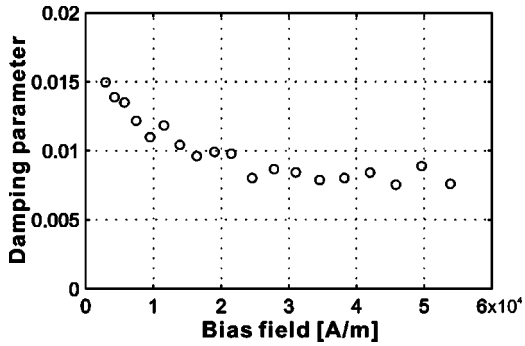

FIG. 4. Dependence of the damping parameter α as estimated by Eq. (10) on the bias field.

$$\zeta = \frac{\omega_M}{(\omega_0 - i\alpha\omega + \omega_M)(\omega_0 - i\alpha\omega) - \omega^2}, \tag{7}$$

where $\omega_0 = \gamma(H_B + H_k)$ and $\omega_M = \gamma M_S$, respectively. In the measurement setup for sample 1, the drive field is almost totally in plane, meaning that only the h_y component needs to be considered. The system is configured to detect only the polar Kerr signal which reflects m_x. Thus, the peak in the amplitude plot of the polar Kerr signal as a function of bias field occurs when the absolute value of P'_{xy} becomes maximum. It can be shown from Eq. (7) that $|P'_{xy}|$ is given by

$$|P'_{xy}|^2 = \frac{(\omega_M \omega)^2}{\{\omega_0^2 + \omega_0\omega_M - (1-\alpha^2)\omega^2\}^2 + (\omega_M^2 + 4\omega^2)\alpha^2\omega^2}. \tag{8}$$

From Eq. (8), assuming that α depends (at most) only very weakly on the bias field around the peak, the peak position $\omega_P = \gamma H_P$ is determined by this equation:

$$\omega_P^2 + \omega_P\omega_M - (1-\alpha^2)\omega^2 = 0. \tag{9}$$

Note that Eq. (9) becomes essentially the same as Eq. (2) under the condition that $H_B + H_k \ll M_S$ since α is much smaller than 1 in permalloy as shown below. The derivative of the phase variation as a function of the bias field at the peak is calculated by differentiating $\phi = \arg(P'_{xy})$ with respect to H_B and substituting H_B with H_P obtained by Eq. (9). This yields

$$\left.\frac{d\phi}{dH_B}\right|_{H_P} = \frac{\gamma}{\omega\alpha}. \tag{10}$$

Using this equation, it is possible to estimate the damping parameter α from the slope of the phase plot of the magnetization response around the resonant peak. Figure 4 shows α estimated by this algorithm. The values of α above 24 kA/m(300 Oe) in this figure are fairly consistent with other studies (0.005,[2] 0.0065,[16] 0.008,[4,12] 0.0097[14]). Below 24 kA/m, α, as determined by the above algorithm, increases as the bias field decreases. This is qualitatively consistent with permeance measurements[6] or time domain inductive measurements.[8,9]

Other studies have attributed the increase of α to spatial inhomogeneities of the local magnetization.[6,13] To examine this notion, the spatial distributions of magnetization response under the resonant condition at three different fre-

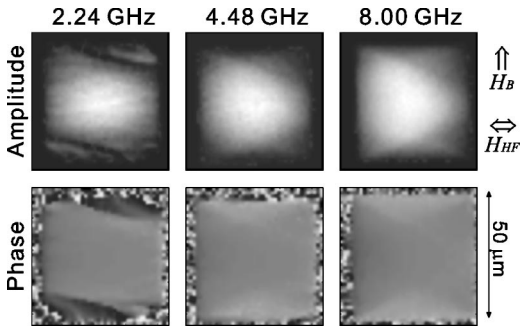

FIG. 5. 2D mapped spatial distribution of the magnetization response under the resonant condition measured at 2.24, 4.48, and 8.00 GHz, respectively. The scan step is 1.38 μm for all images. The amplitude images are normalized by the maximum value of each measurement for the best contrast.

quencies 2.24, 4.48, and 8.00 GHz were captured. Figure 5 shows the results. The top and the bottom rows show the amplitude and phase distribution images, respectively. In the amplitude images, the brightness of each pixel represents the amplitude of the magnetization response at the resonant frequency, meaning that white areas show a large processional motion and black areas have no magnetic activity. In the phase images, black and white areas correspond to $-\pi$ and π relative phase, respectively. As clearly seen, the shape of the dormant areas around the horizontal edges is different among these three frequencies. For example, the image taken at 4.48 GHz has slightly larger dormant areas than that at 8.00 GHz. The amplitude image taken at 2.24 GHz even shows black lines slightly slanted from the horizontal edges, which are believed to be domain walls nucleated under a weak bias field. Furthermore, weak stripe shape amplitude variations running perpendicularly to the bias field are found in this image, which are probably ripple domains. These results clearly demonstrate the correlation between the magnetic inhomogeneities and the apparent increase of α, as suggested by other researchers. Inhomogeneous magnetization distributions should give rise to distributed effective fields or additional coupling to higher order modes, resulting in broadening of the resonant peak. Under this condition, the assumption of coherent rotation, represented by Eq. (1), is no longer valid and therefore the anomalous increase of α in the lower bias field region seen in Fig. 4 should be interpreted as an increase in an *effective* α rather than in the intinsic α. We do not expect the intrinsic α to change over this range of excitation frequencies and/or bias fields.

An important point in using SRFMR-SKEM for estimating the damping parameter should be noted. The peak shape measured as a function of bias field, as shown in Fig. 2, appears too wide to give such a small damping parameter compared to conventional FMR. This is because the plot in Fig. 2 shows the absolute value of magnetization response $|m'+im''|$, while FMR observes m''. As a consequence of this difference, the peak in this measurement tends to be wider than that observed in FMR. Also, FMR observes the energy flow from the drive field to the magnetic system given as $\mu_0 \vec{m} \cdot \vec{h}$. In this integrated sample geometry, the drive field is almost in-plane and therefore only the m_y component contributes to the energy flow. However, SRFMR-SKEM observes the out-of-plane magnetization component m_x which is not directly related to the energy flow. Therefore, the direct comparison of peak shape between SRFMR-SKEM and conventional FMR is not appropriate.

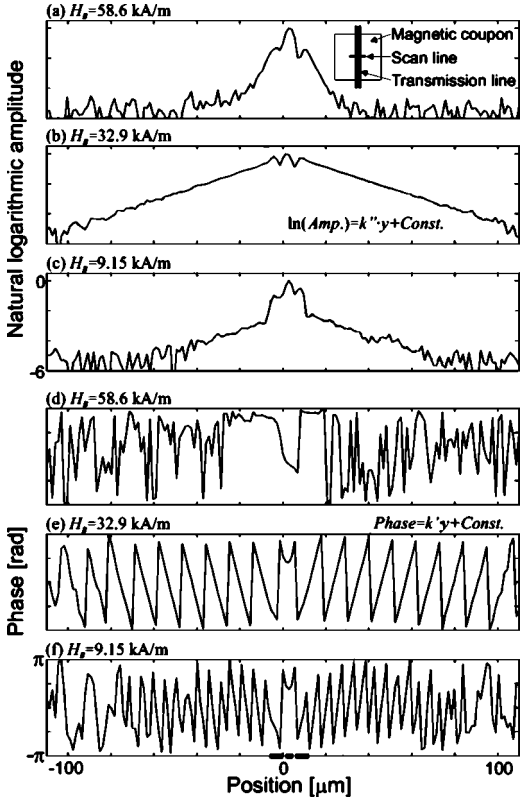

FIG. 6. Line scanned spatial distribution of the magnetization response of 1 mm $\times$ 1 mm square permalloy coupon (sample 2) excited by a localized HF drive field at 8.00 GHz under three bias fields H_B=58.6, 39.2, and 9.15 kA/m. The upper three (a)–(c) and lower three (d)–(f) plots show the amplitude and phase distributions, respectively. Scanning was performed along the center line perpendicular to the transmission line as shown in the inset of plot (a). Three segments of bold lines around the origin at the bottom of the plot (f) show the conductors of the transmission line. The scan step is 1.1 μm for all plots.

B. Sample 2 (localized excitation)

Propagating wave experiments were carried out on sample 2, which has a very large coupon size and a small transmission line width. Figure 6 shows three representative plots of the amplitude and the phase distributions of the magnetization response scanned along the center line of the magnetic coupon perpendicular to the transmission line. These were collected during excitation at 8.00 GHz. The inset in Fig. 6(a) clarifies the scanning orientation. It should be noted that in Fig. 6, the values of amplitude are normalized to the maximum value in each scan. Phase plots are all on the same scale.

In Figs. 6(a) and 6(d) taken at H_B=58.6 kA/m, which is above the field associated with the Kittel mode, well defined amplitude and phase distributions are confined near the

transmission line and no propagating waves are observed outside of the excitation area. For bias fields below the Kittel mode resonant point, propagating plane waves are clearly seen with an exponential amplitude decay as indicated by the linear slopes outside of the excitation area in the natural logarithmic amplitude plot with position [Figs. 6(b) and 6(c), respectively]. Further evidence is provided by the sawtooth like phase variations seen in Figs. 6(e) and 6(f), respectively. These are the result of a linear phase variation wrapped around at every 2π. Also clearly observed in Figs. 6(c) is the asymmetric amplitude distribution between the waves propagating in the positive and negative y directions.

A simple estimation of the strength of the exchange coupling relative to the magnetostatic coupling is presented here, to justify the assumption that the magnetostatic coupling is dominant in this experiment. The angular frequency of the exchange mode spin wave ω_e is given by[22]

$$\hbar\omega_e = 2SJ_{\mathrm{ex}}a^2k^2, \tag{11}$$

where S is the quantum number of the electron spin, J_{ex} is the exchange integral, and a is the lattice constant. J_{ex} can be approximately estimated as

$$J_{\mathrm{ex}} = 4\Theta_C k_B/z, \tag{12}$$

where Θ_C is Curie temperature, k_B is Boltzmann constant, and z is the number of nearest neighbor spins. From Eqs. (11) and (12) and the values typical for permalloy ($S=1/2$, $\Theta_C=983$ K, $z=12$, and $a=3.55$ Å), the wavelength which gives the resonant frequency of 2 GHz, the lowest frequency in this work, is estimated as 130 nm. This is significantly smaller than the highest spatial resolution of the current SRFMR-SKEM configuration. From this estimation, it is assumed in this work that the exchange coupling can be ignored and only the magnetostatic coupling is considered in the following discussion.

According to the DE model for magnetostatic mode waves propagating in a lossless magnetic slab,[15] the MSSW exists when a bias field weaker than that required for the Kittel mode is applied. Under the condition of $k_z=0$, all the magnetostatic volume mode waves (MSVW's) degenerate to the natural frequency of the Kittel mode in the magnetostatic approximation and therefore no mode should exist under the application of a bias field stronger than for the Kittel mode. This degeneracy also leads to zero group velocity of MSVW's, meaning that these modes cannot propagate perpendicularly to the bias field. Thus, we interpret the observed response around the excitation area in Figs. 6(a) and 6(d) at $H_B=58.6$ kA/m as the Kittel mode or MSVW's excited through finite damping and the other two cases at lower bias fields as pure MSSW's. The source of the asymmetric amplitude distribution observed in Figs. 6(c) is considered to be the field displacement nonreciprocity of the MSSW also predicted in the DE model, which becomes more prominent when the wave number becomes larger. Note that these figures are on log scales covering $e^6 \sim 400$ of amplitude range such that the small difference observed in Fig. 6(c) is in fact significant. The amplitude decay with propagation distance cannot be predicted by the original DE model, and is discussed below.

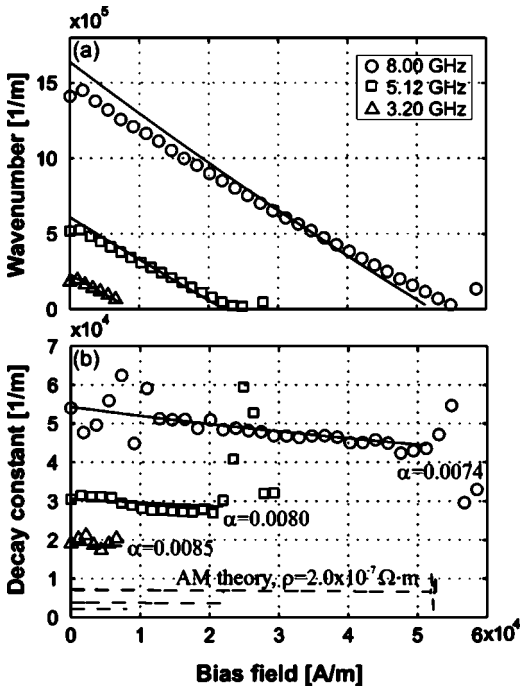

FIG. 7. Dependence of the wave number and decay constant (the real and imaginary part of the complex wave number) of the MSSW excited in sample 2 on the bias field. The circles, squares and triangles show the experimental results at 8.00, 5.12, and 3.20 GHz, respectively. Solid lines are theoretical values calculated by the extended DE model (16). α of 0.0074, 0.0080, and 0.0085 are used for the theoretical calculation of both the wave number and decay constant at each of the three frequencies. Also shown in (b) as three broken lines are decay constants calculated by the Almeida and Mills (AM) theory, assuming the damping parameter, $\alpha=0$ and the volume resistivity $\rho=2\times10^{-7}$ Ωm.

This measurement was made at three excitation frequencies 8.00, 5.12, and 3.20 GHz, while sweeping the bias field. The wave number and the decay constant at each measurement point were determined from the slope of the phase and the natural log of the amplitude distribution plots assuming that the MSSW obeys the form of a simple decaying plane wave

$$\vec{m} = \vec{m}_0 \exp i\{(k_y' + ik_y'')y - \omega t\}, \tag{13}$$

where k_y' and k_y'' are the wave number and the decay constant along the y axis, respectively. These correspond to the real and imaginary part of the complex wave number. The amplitude and phase distribution in the positive side between 20 μm-60 μm from the origin are used for linear fitting to avoid the influence of the complicated magnetization profile around the excitation area due to the coplanar transmission line geometry, and the noise which becomes dominant when the magnetization response becomes too weak. Figures 7(a) and 7(b) show the dependencies of k_y' and k_y'', determined according to this method, on the bias field. Also shown in these figures as solid lines are theoretical values of k_y' and k_y'' computed by the following extension of the DE model to include finite damping.

When a finite α is introduced in the LLG equation as in Eq. (1), the Polder susceptibility tensor P is given by substituting Eqs. (4) and (5) into Eq. (1), assuming that the dynamic terms are much smaller than the static terms and dropping second order terms

$$\vec{m} = P\vec{h},$$

$$P = \begin{pmatrix} \chi & -i\kappa \\ i\kappa & \chi \end{pmatrix},$$

$$\chi = \frac{(\omega_0 - i\alpha\omega)\omega_M}{(\omega_0 - i\alpha\omega)^2 - \omega^2},$$

$$\kappa = \frac{\omega\omega_M}{(\omega_0 - i\alpha\omega)^2 - \omega^2}. \tag{14}$$

This is equivalent to replacing ω_0 with $\omega_0 - i\alpha\omega$ in the formal definition of the Polder susceptibility tensor for a lossless magnetic system.[23] The dispersion relation of the MSSW propagating along the y axis in the original DE model is given by

$$\omega^2 = \omega_0(\omega_0 + \omega_M) + (\omega_M^2/4)\{1 - \exp(-2k_y d)\}, \tag{15}$$

where k_y is the real wave number along the y axis and d is the film thickness. It can be shown that the DE formalism holds even with a susceptibility tensor having a complex ω_0. This means that the dispersion relation derived by the original DE model (15) can, in general, take a complex ω_0. Thus, the real and imaginary part of k_y are obtained by solving Eq. (15) with respect to k_y and substituting ω_0 with $\omega_0 - i\alpha\omega$. That is,

$$k_y' + ik_y'' = -\frac{1}{2d}\ln\left[1 - 4\frac{\omega^2 - (\omega_0 - i\alpha\omega)(\omega_0 - i\alpha\omega + \omega_M)}{\omega_M^2}\right]. \tag{16}$$

The damping parameter α was used as a fitting parameter in this calculation and the best agreement was obtained with a value of 0.0074 for 8.00 GHz, 0.0080 for 5.12 GHz, and 0.0085 for 3.20 GHz, respectively, as shown in Fig. 7(b). It should be noted that the k_y' curves in Fig. 7(a) depend very weakly on α, meaning that k_y' calculated by Eq. (16) is essentially the same as that calculated by the original DE model dispersion relation (15). On the other hand, the k_y'' curves shown in Fig. 7(b) are very sensitive to the value of α and would be zero if α were set to zero. Therefore the determination of α was performed solely by fitting to the k_y'' data on Fig. 7(b). The agreement of the wave number k_y' between the theory and the experimental results is fairly good, with small disagreement in the slope and intersection with the axes. This disagreement is possibly caused by errors associated with the parameters used in the theoretical calculation of k_y', since all the parameters are given by other measurements and no fitting process is used.

The decay constant k_y'' also shows fairly good agreement between the theory and experimental results if the bias field is neither very close to the Kittel mode resonant point (the bias field which gives $k_y' = 0$) nor very weak. Under these extreme conditions, the amplitude of the MSSW outside of the excitation area becomes very weak and is subject to the stray HF drive field or the noise floor level. For this reason, the fitting results tend to show some deviation from the real decay constant of the propagating MSSW and therefore are not very reliable under these conditions. The values of α obtained by fitting to k_y'' in the measurement on sample 2 are reasonably consistent with the values estimated in the Kittel mode measurements on sample 1 for bias fields higher than 24 kA/m, and do not show very strong dependence on either bias field or frequency. In the experiment on sample 2, the static domain structure and the internal field distribution are expected to be fairly uniform under wide range of bias fields, due to its much higher aspect ratio compared to sample 1. This is considered to be the reason why α does not change much over a wide range of bias fields.

Silva *et al.* studied the magnetic flux propagation in a 250 nm thick permalloy film. They observed that it propagates with a frequency of 1.54 GHz under a bias field of 80 A/m. It also displayed a characteristic decay length of about 150 μm ($k'' = 6.7 \times 10^3$ m^{-1}).[24] If the extended DE model (16) is applied to their experimental conditions and observations ($g = 2.02$, $d = 250$ nm, $f = 1.54$ GHz, and $k'' = 6.7 \times 10^3$ m^{-1}), the resulting value of α is 0.015. This is in fair agreement with the value of α at lower bias fields seen in Fig. 4, but somewhat larger than their estimation in Ref. 24 that $\alpha = 0.01$. Even this level of agreement may appear surprising at first, considering the fact that they were using a very large drive field to attempt to show nonlinear effects, while the drive field in this work is very weak. However, Covington *et al.* reported that the magnetization dynamics remain linear even when very high excitation fields are applied to the magnetic sample.[14] Based on these observation results, the simple extension of the DE model presented in this work may have a wide range of applicability for predicting the decay of MSSW's, even when the amplitude is quite large.

A final comment about the source of relaxation is included here for completeness. Almeida and Mills (AM) calculated the complex wave number of the MSSW propagating along the y axis in a conducting magnetic material where losses were due to eddy currents, and α was assumed to be zero.[25] The decay constants calculated by this model using a resistivity of 2×10^{-7} Ω m(20 $\mu\Omega$ cm), which is a typical value for sputtered permalloy, and numerically solving Eq. (2.11) in Ref. 25, are also shown for comparison in Fig. 7(b) as broken lines. The AM theory says that if the decay of the MSSW is caused purely by eddy current loss, the decay constant should be much smaller than the observed result. This means that although it is true that ferromagnetic metal systems are generally much more heavily damped than ferrimagnetic insulators such as YIG or ferrite, a classical eddy current damping theory cannot account for the decay of the propagating MSSW.

Heinrich *et al.* reviewed the mechanisms of magnetic relaxation in ferromagnetic metals.[26] There are three principle ones discussed, namely, eddy current damping, magnon-phonon coupling, or phonon drag and spin-orbit relaxation. Our analysis using the AM theory suggests that eddy currents contribute at most about 15% of the observed decay at

8 GHz and even less than this at lower frequencies. According to the analysis in Ref. 26, the expected contribution from eddy currents to FMR line width is approximately 40%. This discrepancy may be due to the fact that FMR operates under resonant conditions in which the permeability is enhanced. This may artificially shrink the skin depth and allow a greater contribution from eddy currents to FMR linewidth than to the decay of propagating spin waves. McMichael *et al.* estimated the contribution of magnon-phonon coupling through anisotropy and magnetostriction to damping in permalloy and have concluded that it, too, is too small to explain the observed results.[27] Recently, Ingvarsson *et al.* have measured damping in permalloy films at room temperature as a function of film thickness and found a strong correlation between film resistance and damping.[28] Damping increased with increasing resistivity regardless of thickness, which is exactly the behavior expected in the spin relaxation model. Using the analysis of Kambersky *et al.*, and a simple Drude model of permalloy, they conclude that spin-orbit coupling can quantitatively explain a damping parameter α of 0.008 for permalloy with the resistivity of a relatively thick film of 24 $\mu\Omega$ cm, with one necessary assumption.[29] This assumption is that 10% of electron scattering events result in a spin flip. This number is reasonable and consistent with spin diffusion lengths in permalloy as discussed in Ref. 26. Ingvarsson also ruled out two-magnon scattering in explaining their damping. These numbers are all quantitatively consistent with our own experiments, allowing the conclusion that the observed dacay length of the MSSW observed in this work is mainly caused by spin-orbit relaxation.

IV. CONCLUSION

In conclusion, detailed studies of two different modes of magnetic excitation on permalloy films were performed with a recently introduced measurement technique based on a scanning Kerr microscopy (SRFMR-SKEM). In the uniform excitation experiment, the resonant condition of the observed excitation agreed well with the conventional Kittel mode equation, but the damping parameter showed strong dependence on the bias field. Measurement of the spatial distribution of the magnetization response clarified that the change of the static domain structure and possibly the ripple domain formation are responsible for this increase.

In the localized excitation experiment, propagating MSSW's were observed. The wave number and decay constant estimated from the line scanned distribution of the magnetization response showed fairly good agreement with the DE model, when it was extended to include a finite damping parameter. The values of α estimated in this measurement were reasonably consistent with the result of the uniform excitation measurement at higher bias fields. The comparison of the experimental data with the AM theory suggested that the eddy current probably has only a modest effect on the decay of the MSSW in this sample.

ACKNOWLEDGMENTS

The author would like to thank Josh Schare for the finite element method calculation of the bias field distribution and Seungook Min for preliminary sample fabrication. This work was supported, in part, by the National Science Foundation under Grant No. ECD-8907068.

*Email address: stamaru@andrew.cmu.edu

[1] S. Chikazumi, *Physics of Ferromagnetism*, 2nd ed. (Oxford University Press, Oxford, 1997).
[2] C. E. Patton, A. Frait, and C. H. Wilts, J. Appl. Phys. **46**, 5002 (1975).
[3] D. Bastian and E. Biller, Phys. Status Solidi A **35**, 113 (1976).
[4] S. Mizukami, Y. Ando, and T. Miyazaki, Jpn. J. Appl. Phys., Part 1 **40**, 580 (2001).
[5] W. D. Doyle, X. He, P. Tang, T. Jagielinski, and N. Smith, J. Appl. Phys. **73**, 5995 (1993).
[6] T. J. Klemmer, K. A. Ellis, and B. van Dover, J. Appl. Phys. **87**, 5846 (2000).
[7] W. P. Jayasekara, J. A. Bain, and M. H. Kryder, IEEE Trans. Magn. **34**, 1438 (1998).
[8] T. J. Silva, C. S. Lee, T. M. Crawford, and C. T. Rogers, J. Appl. Phys. **85**, 7849 (1999).
[9] G. M. Sandler, H. N. Bertram, T. J. Silva, and T. M. Crawford, J. Appl. Phys. **85**, 5080 (1999).
[10] T. J. Silva and T. M. Crawford, IEEE Trans. Magn. **35**, 671 (1999).
[11] T. M. Crawford, M. Covington, and G. J. Parker, Phys. Rev. B **67**, 024411 (2003).
[12] W. K. Hiebert, A. Stankiewicz, and M. R. Freeman, Phys. Rev. Lett. **79**, 1134 (1997).
[13] N. M. Salansky, B. P. Khrustalev, A. S. Melnik, L. A. Salanskaya, and Z. I. Sinegubova, Thin Solid Films **4**, 105 (1969).
[14] M. Covington, T. M. Crawford, and G. J. Parker, Phys. Rev. Lett. **89**, 237202 (2002).
[15] R. W. Damon and J. R. Eshbach, J. Phys. Chem. Solids **19**, 308 (1961).
[16] M. Bailleul, D. Olligs, C. Fermon, and S. O. Demokritov, Europhys. Lett. **56**, 741 (2001).
[17] W. K. Hiebert, G. E. Ballentine, and M. R. Freeman, Phys. Rev. B **65**, 140404 (2002).
[18] J. P. Park, P. Eames, D. M. Engebretson, and P. A. Crowell, Phys. Rev. Lett. **89**, 277201 (2002).
[19] S. Tamaru, J. A. Bain, R. van de Veerdonk, T. M. Crawford, M. Covington, and M. H. Kryder, J. Appl. Phys. **91**, 8034 (2002).
[20] P. H. Briant, J. F. Smyth, S. Schultz, and D. R. Fredkin, Phys. Rev. B **47**, 11 255 (1993).
[21] *Magnetic Oxides Part 2*, edited by D. J. Craik (Wiley, New York, 1975).
[22] C.-W. Chen, *Magnetism and Metallurgy of Soft Magnetic Materials* (Dover, London, 1986).
[23] D. D. Stancil, *Theory of Magnetostatic Waves* (Springer-Verlag, Berlin, 1993).
[24] T. J. Silva, M. R. Pufall, and P. Kabos, J. Appl. Phys. **91**, 1066 (2002).

[25] N. S. Almeida and D. L. Mills, Phys. Rev. B **53**, 12 232 (1996).
[26] B. Heinrich, R. Urban, and G. Woltersdolf, IEEE Trans. Magn. **38**, 2496 (2002).
[27] R. D. McMichael and A. Kunz, J. Appl. Phys. **91**, 8650 (2002).
[28] S. Ingvarsson, L. Ritchie, X. Y. Liu, G. Xiao, J. C. Slonczewski, P. L. Trouilloud, and R. H. Koch, Phys. Rev. B **66**, 214416 (2002).
[29] J. Kunes and V. Kamabersky, Phys. Rev. B **65**, 212411 (2002).